IEEE Access
Multidisciplinary ⋮ Rapid Review ⋮ Open Access Journal

Received December 10, 2020, accepted December 23, 2020, date of publication December 28, 2020,
date of current version January 5, 2021.

Digital Object Identifier 10.1109/ACCESS.2020.3047736

A Method for Infrared Sea-Sky Condition Judgment and Search System: Robust Target Detection via PLS and CEDoG

DONGDONG MA, LILI DONG, (Member, IEEE), AND WENHAI XU
School of Information Science and Technology, Dalian Maritime University, Dalian 116026, China

Corresponding author: Lili Dong (donglili@dlmu.edu.cn)

This work was supported in part by the National Natural Science Foundation of China under Grant 61701069, and in part by the Fundamental Research Funds for the Central Universities of China under Grant 3132019340 and Grant 3132019200.

ABSTRACT It has always been a serious challenge to efficiently detect infrared targets from remote sea-sky background without any prior knowledge. This is especially true when target features of different areas are irrelevant in the same image. The main contribution of this paper is to design an algorithm of judge sea-sky condition and detect infrared target, in which a two-direction local maximum (TLM) method and peak local singularity (PLS) is proposed, constant excitatory difference of Gaussians (CEDoG) operator is applied by analyzing the characteristics of the target. First and foremost, the TLM method is adopted to refine sea-sky area to extract the suspected sea-sky line, and design the strategy of ''de-false'' to realize the accurate determination of the sea-sky line. Secondly, small targets in the sea-sky area (pixels 2×2 to 9×9) are detected by applying the PLS method. Finally, CEDoG filtering method is used to suppress the background and improve the significance of the target, and high threshold OTSU method (H-OTSU) is applied to find the most significant area and self-designed area growth rule to ensure the accuracy and integrity of the maritime area target detection. Comparing with the other state-of-the-art methods in the experiments, our strategy has a robust and effective performance in terms of recall, precision, elapsed time, complexity, detection and false alarm rate.

INDEX TERMS Judge sea-sky background, maritime surveillance, infrared target detection.

I. INTRODUCTION

With the development of economy and science and technology, maritime activities continue to increased due to the complex and volatile marine environment. The detection, identification and tracking of targets at long distances at sea has always been a difficult and bottleneck problem in modern military and civilian fields. Detecting small and multiple targets of unknown position and velocity at a complex environment is an important issue in infrared search and track (IRST) system. This is a necessary application to warn from incoming maritime targets from a distance. In recent years, marine search and rescue equipment mainly consists of visible light cameras and infrared cameras. Infrared cameras have the advantages of strong fog permeability, long shooting distance, and the ability to work day and night compared with visible light cameras. Therefore, IRST systems have become the main method for detecting remote range maritime target. The sea-sky environment with uncertain background clutter and wave noise is still the most prone to occur, which brings great difficulties and challenges to long range maritime targets detection. At present, it has been studied and discussed by a large number of scholars. Table 1 lists some state-of-the-art maritime target detection methods for the sea-sky environment. Aghaziyarati *et al.* [1] proposed proper weighting coefficients which are derived from the cumulative directional derivatives to eliminate the deficiencies of the average absolute gray difference (AAGD) algorithms. Experiments evaluated on real images confirmed the practicability and accuracy of near sea-sky location targets. Kong *et al.* [5] analyzed the weak and small targets in the sea-sky environment where the target is far away from the detector, and puts forward the idea based on multi-scale, detect the sea-sky horizontal line according to gray level image in approximate sub image with low frequency. Using the mutual wavelet energy combination algorithm to detect the small maritime

The associate editor coordinating the review of this manuscript and approving it for publication was Ravibabu Mulaveesala.

TABLE 1. State-of-the-art methods for improving the IRST system performance in sea-sky environments.

Infrared Target Detection Methods Under Sea-sky Background	Extraction Direction Method	[1]-[4]
	Wavelet Transform Method	[5]-[7]
	Based on Gray and Contrast	[8]-[9]
	Visual Attention Model	[10]-[14]
	Multiscale Fuzzy Metric	[15]-[16]

TABLE 2. State-of-the-art methods for improving infrared small target detection.

Infrared Small Target Detection Methods	Local Contrast Method	[17]-[20]
	Spatio-temporal Saliency Approach	[21]-[22]
	Low-rank Tensor Completion	[23]-[24]
	Based on Deep Learning	[25]-[29]

targets successfully. Although the above method can detect the target accurately, it has low discrimination of strong wave clutter, which leads to a high false alarm rate. Lu *et al.* [8] considered complex sea-sky environment of the target detection problem, an edge extraction algorithm based on grayscale corrosion is adopted, the comprehensive utilization of gray filling to achieve the goal of edge connection. At the same time, the target is identified by the maximum connected area labeling method. Dong *et al.* [10] proposed an adaptive morphological selection method, and replaced the image boundary saliency attenuation strategy in the original visual attention model with the boundary saliency retention strategy. Combined with the adaptive binarization method, a small target is accurately detected under sea-sky condition. However, the above methods are easily affected by clouds and islands, which will lead to a higher missed alarm rate of the small target detection results. Deng *et al.* [15] presented an effective method for detecting small infrared targets embedded in complex backgrounds through a multiscale fuzzy metric model that measures the certainty of targets in images. Firstly, a lot of background clutter and noise are eliminated by using fuzzy metric, and then a simple adaptive threshold was used to segment the target. Although this method is effective, it will be affected by high brightness noise.

To comprehensively show the superiority of the presented method, more recent infrared small target detection methods are systematically reviewed in the Table 2. Chen *et al.* [17] applied a method based on local contrast, they used the brightness difference between the target and its neighboring area to detect the target. Li *et al.* [21] proposed a spatio-temporal saliency model to solved the infrared dim moving target detection problem. Although above method is effective, it will be affected by high brightness noise. To improve the detection ability of infrared small targets in complex backgrounds, Zhang *et al.* [23] proposed a novel method based on non-convex rank approximation minimization joint l2,1 norm. However, its robustness is insuffieient under noisy and complex situations. Li *et al.* [25] proposed a weakly supervised deep learning (WSDL) method for multi-class geospatial targets detection using scene-level tags only. Tao *et al.* [26] proposed a scene context-driven targets detection method. At first perform scene classification using the deep learning method and then detect vehicles in roads and parking lots separately through different vehicle detectors. Raimon *et al.* [27] proposed a new spatiotemporal learning approach based on a deep learning segmentation model that detects targets directly from a series of frames. Although the above methods can work well in sea-sky background, the quality of selected features and training samples could evidently influence the detection results. Target will not be well distinguished if the finite training samples are insufficient to involve enough information. In addition, the deep learning method will consume more time.

It can be known from above scientific research situation that these current methods are more suitable for targets with a single feature in the entire image [30]–[34]. On the other word, sea-sky background clutter and wave noise in the space or transform domain are irrelevant to the target [9], [35]–[40].

The main challenge currently encountered is when the distance between different targets and the imaging system may be different, so infrared thermal imaging camera receives different radiant energy during the actual detection process. The target at the sea-sky area captured in the infrared image is small and obscure, closer to the imaging system are larger and sharper. As a result, the target no longer has a single characteristic. This brings greater challenges to far-range target detection in the sea-sky environment. In view of this situation, there is no specific solution after consulting the literature. Therefore, this paper proposed a new strategy of infrared sea-sky environment search system by collecting the required experimental data and analysis to achieve accurate detection of any targets.

The main contributions of this paper are as follows: (1) Position features, edge contour features, pixel features, grayscale features, contrast features and unique features of sea-sky conditions of the target are analyzed and a new method of area division is designed. (2) A TLM method is proposed to refine the sea-sky area to extract suspected sea-sky line, and a "de-false" strategy is designed to accurately judge the sea-sky environment. (3) A PLS method is applied to accurately detect weak targets in the sea-sky areas (pixels are 2×2 to 9×9). (4) For maritime area, CEDoG filtering method is used to suppress the background and improve the saliency of the target, and the H-OTSU method is selected to find the most significant area and the set area growth rule to ensure accuracy and integrity of target detection. These four contributions make the proposed algorithm can accurately detect infrared targets with different characteristics in different sea -sky environments.

The remaining part of this paper is organized as follows. In Section II, characteristics of target and background

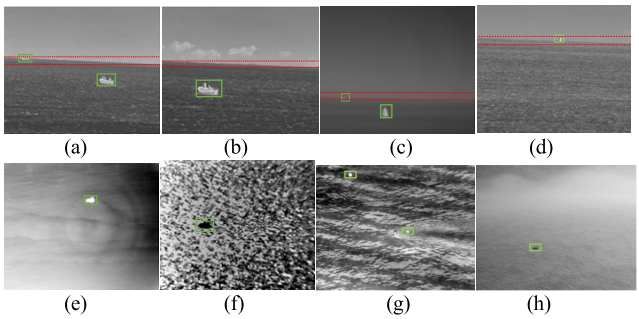

FIGURE 1. Representative IR images taken in complex backgrounds. (a)-(d) Sea sky background. (e) Calm sea. (f) Backlighting environment. (g) Big storm. (h) Sea fog.

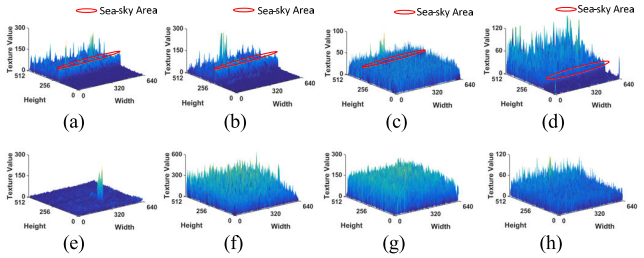

FIGURE 2. Three-dimensional texture feature distribution of IR images in Fig.1 respectively.

are analyzed and described under sea-sky environment. Section III introduces elaborate steps of the proposed method, including judgment and extraction of sea-sky line, sea-sky area target detection method and maritime target detection process. In Section IV, several experiments on data sets and relative discussions are presented to demonstrate the efficiency of the proposed strategy. An overall conclusion is drawn for a summary of this paper in Section V.

II. IMAGE CHARACTERISTICS ANALYSIS

We selected four infrared images under different sea-sky scenarios for feature analysis, as shown in Fig.1(a) - (d). Among them, there are two targets in Fig.1 (a) and (c), one is far from the thermal imager in the sea-sky area, and the other is closer to the infrared camera in the maritime area. Fig.1(b) and (d) each have one target, located in the maritime area and the sea-sky area respectively. The above four situations include all potential locations of the target in the sea-sky environment. In order to more accurately analyze the unique characteristics, we also discuss infrared images in four common scenes, which are infrared images taken under normal conditions, backlighting environment, wind and wave and sea fog. The images are shown in Fig.1 (e) - (h). This provides the possibility to distinguish the sea-sky environment from other complex environments. All the above infrared images are taken by medium wave refrigeration infrared camera with a band of 3.7-4.8um and a resolution of 640 * 512. For the convenience of observation, the target is marked by a green box.

First of all, we can obviously see that sea-sky environment can be roughly divided into three areas from Fig.1 (a)-(d), sky area, sea-sky area and maritime area respectively. As shown in the red line division area (the segmentation rules will be introduced in Section III). Secondly, there will be a horizontal or inclined sea-sky line that runs through the entire image. The potential location of the target is the sea-sky area and maritime area. For the images taken in the Fig.1 (e)-(h) environments, it can be seen that there is only one maritime area and target appears only in the maritime area. Besides, in order to analyze more comprehensively, this paper analyzes the texture features in the horizontal direction of the entire image. Convolution of original image with [1/6 1/6 1/6; 0 0 0; -1/6 -1/6 -1/6] operator to extract horizontal coarse texture information. The three-dimensional result obtained is shown in the Fig.2 and there are always continuous and strong texture features along a certain direction (marked by the red curve) in sea-sky environments. However, for other complex environments there will not be significant and continuous texture features in one direction. This unitary feature provides us with the possibility to distinguish the sea-sky environment from other complex sea condition. This paper analyzes the grayscale features of image, gray histograms of the entire image and three areas is calculated, as shown in Fig.3 (a) (b) (e) (f) and (c) (d) (g) (h) respectively.

Observation Fig.3 (a) and (e) shows that, first of all, target on the sea-sky line is far away from the infrared camera, the size of the target is smaller than that maritime target. For example, the number of pixels of target on the maritime area in Fig.3 (a) and (e) is 832 and 390 respectively. The number of pixels of target on the sea-sky area is 54 and 40 respectively. Therefore, the contour information of maritime area target is clearer than sea-sky area target, that is, the contour information and size of the target in different area are not same. Secondly, the emissivity and reflectivity of ships are also different because of the diverse materials of ships on the sea. According to Planck rule [41], radiant energy of targets is also variable. Therefore, it may appear that gray value of the sea-sky area target is greater or less than maritime area target. As shown in Fig.3 (a) gray range of the sea-sky target is 161-182, and the gray range of the maritime target is 153-198. In Fig.3 (e), the gray range of sea-sky target is 117-121, and the gray range of maritime target is 109-180. Therefore, the gray level of target in multiple areas may be distinctive. Third, it can see that the gray range of the maritime target is 153-198, and the gray range of the sea wave is 81-195 from Fig.3 (b). The gray range of the target at sea-sky is 156-168, and the gray range of the sea wave is 89-162 from Fig.3 (f). We can find that sea wave is still a common interference. Fourth, because it is easier to be disturbed by the sky or clouds in the sea-sky environment, it can be found that Fig.3 (c) the gray range of the sky is 136-194 and gray range of the maritime target is 153-198. The gray range of the cloud in the sky is 160-209, and that of the maritime target is 130-226 from in Fig.3 (d). It can be seen from that the sky or cloud has similar intensity to the target, which will bring interference to the detection of maritime or sea-sky targets. Therefore, no matter when the target appears at the same time or separately in the sea-sky

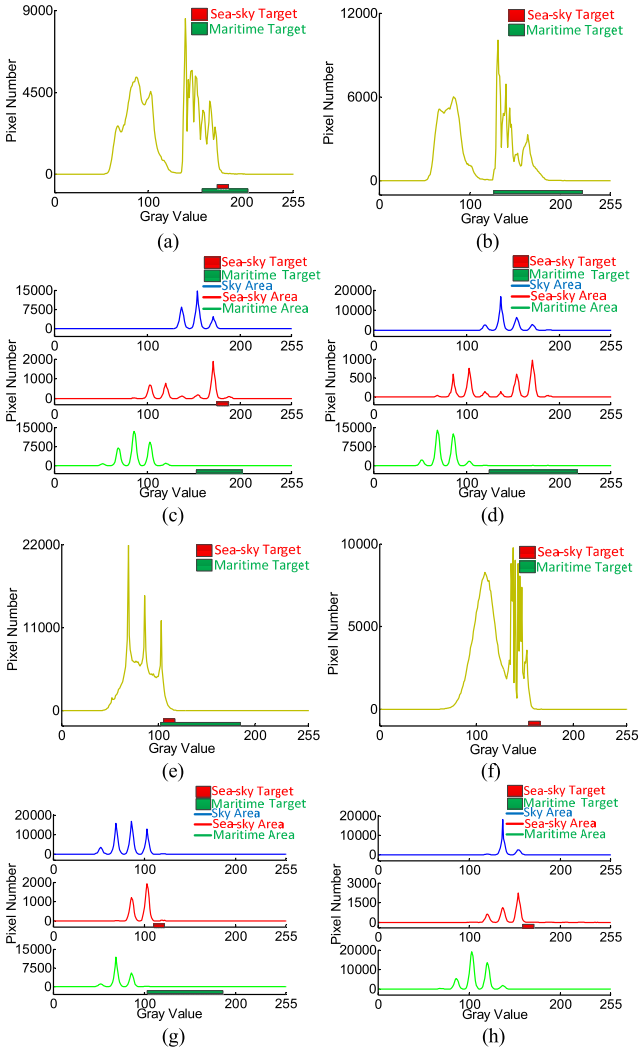

FIGURE 3. Gray distribution histogram of whole image and each area in the sea sky environment for Fig. 1(a)-(d). ((a) (b) (e) (f): Gray distribution histogram of the whole image for Fig. 1 (a)-(d). (c) (d) (g) (h): The histogram of gray distribution of each area in Fig. 1 (a)-(d).)

and maritime area, the intensity of the target is mixed in the noise of waves, clouds and so on, and there is no unique feature of the target that can be found. When we separate the three areas, we further analyze the sea-sky area in Fig. 3 (c) (g) (h). Gray value range of the target is the largest in the whole sea-sky area, and target has the strongest contrast features. For the maritime area in Fig.3 (c) (d) (g), there are 179, 211 and 57 clutter pixels in the same gray range or even larger than the gray value of the target. Interference is the sea wave clutter, which is smaller than the size of target and at the highest frequency.

Therefore, from the above analysis of the sea-sky environment in this paper, sea-sky condition always has continuous and significant texture feature along a certain direction compared with other complex environments. The location of the target mainly appears in the sea-sky area and the maritime area. The sea-sky area is usually a small target and target has significant gray and contrast characteristics. In the maritime area, the target is usually large and the edge contour is relatively clear, and it is often accompanied by wave clutter interference, which is smaller than the target size. According to the analysis results, this paper proposed target detection algorithm suitable for each area in the Section III.

III. PROPOSED ALGORITHM

In this chapter, it is divided into the following three parts, which are judge and extract sea-sky line method, the sea-sky target detection method and maritime target detection method. Overall flow chart of algorithm is shown in Fig. 4.

A. SEA-SKY LINE DETECTION METHOD AND AREA SEGMENTATION RULES

According to the analysis in Section II, the unique feature of the sea-sky environment is that it has continuous and strong texture features along a certain direction. Therefore, this paper proposed a series of "wavelet denoise + extract texture features + judge and extract sea-sky line" strategy. As shown in Fig.5. Wavelet denoising is based on haar's wavelet base to perform wavelet decomposition of the original image to obtain low-frequency images. It has eliminated the influence of high-frequency noise to improve image quality and contrast of the target. First, proposed method in this paper to extract texture features consists of extracting horizontal coarse texture information, root mean square estimation threshold method and two-direction local maximum method. We apply the [1/6 1/6 1/6; 0 0 0; -1/6 -1/6 -1/6] operator to convolve low-frequency images to transform the spatial domain into the gradient domain to obtain all rough texture information RT. In order to eliminate some sea wave clutter interference, this paper uses the root mean square estimation threshold method to determine the minimum cutoff value of texture information, which is as follows:

$$Thresh = \sqrt{scale \cdot \frac{\left(\sum_{i=1}^{h} \sum_{j=1}^{w} \left(RT(i,j)^2\right)\right)}{(h \cdot w)}} \tag{1}$$

Scale directly determines the size of the threshold. If the scale is too large, there will be discontinuities at the sea-sky line after the threshold, which will affect the accuracy of subsequent sea-sky line extraction. Experiments have found that the effect is better when the scale is 4. h and w expressed as the height and width of the image. Thus, in order to find sea-sky candidate area, mask image Mask (i, j) is given by:

$$Mask(i,j) = \text{Bool}(|RT(i,j)| > Thresh) \tag{2}$$

In order to achieve the purpose of accurately locating the sea-sky line, this paper proposed an idea to further refine sea-sky texture information by finding local maximum in two directions. Firstly, image after the root mean square estimation threshold is used as a mask and multiplied by the wavelet denoised image WN to obtain the region of interest (ROI) in the spatial domain of the original image, WD is the image in wavelet domain after threshold, candidate area image CR is calculated as follows:

$$CR(i,j) = WD(i,j) \&\& WN(i,j) \tag{3}$$

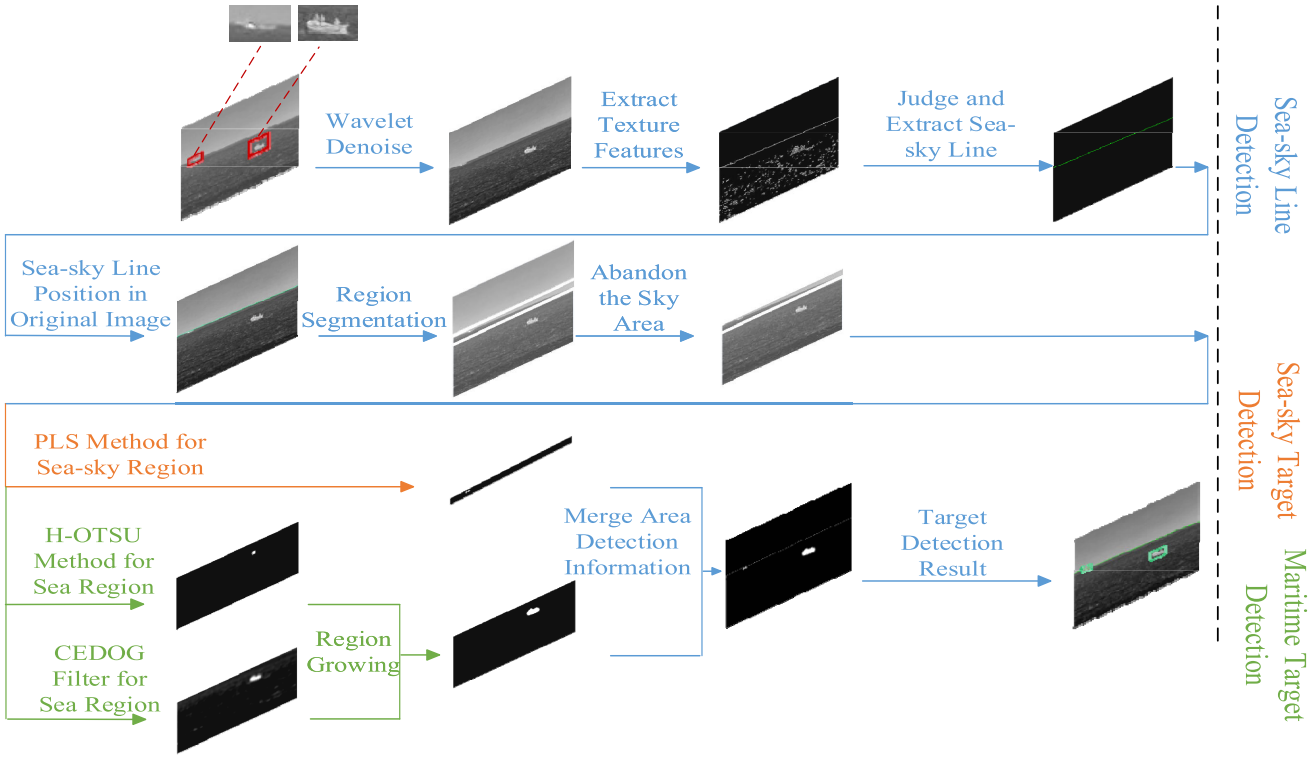

FIGURE 4. The overall framework of the proposed method composed of sea-sky line detection, sea-sky target detection and maritime target detection.

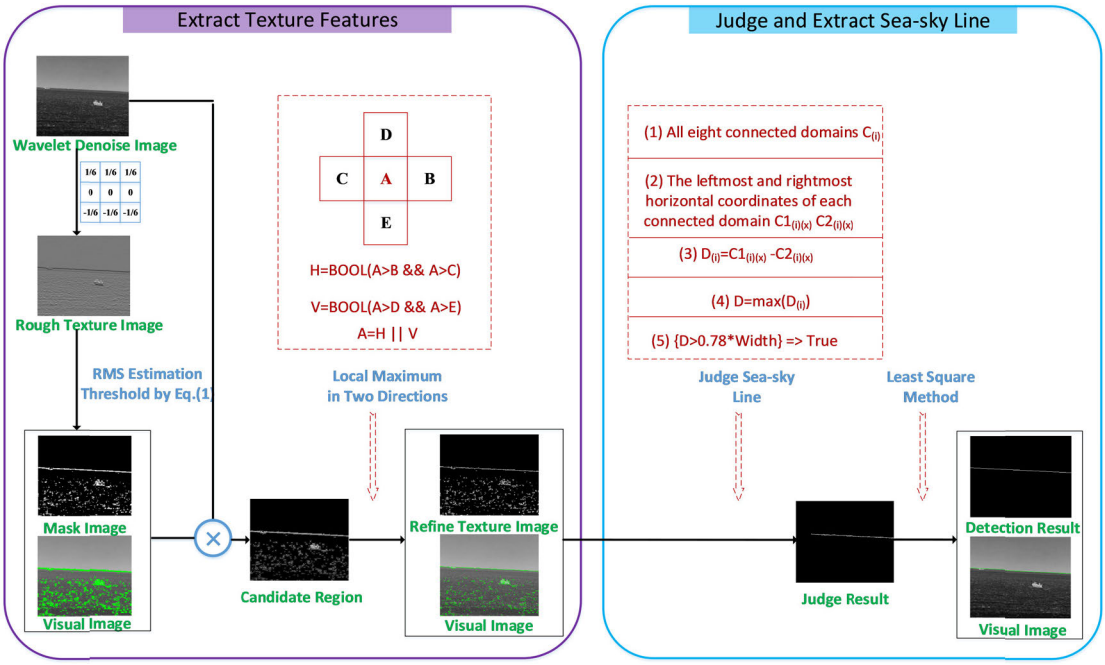

FIGURE 5. Flow chart of sea sky line identification and detection.

Then the first point of interest in the upper left corner of ROI is taken as the reference origin, and the relationship between horizontal or vertical direction of the reference point and value of the reference point is analyzed. If the reference point has the largest gray value in either direction, it is regarded as the suspected reference point of the sea-sky line. We get refine texture image after above processing. Through the observation of the visualization results and statistics, it is found that only 71 pixels deviate from the sea-sky line position. On the contrary, 815 pixels before the processing. Therefore, proposed method is extremely advantageous for the accurate positioning of sea-sky line. Secondly, considering that the waves move in the form of periodic waves, the gray distribution in the image should also exist in the

form of waves, so texture features at the waves are also more significant. In order to distinguish the sea-sky line and eliminate the wave interference to achieve the purpose of ''de-false'', This paper calculates all eight connected domains of the texture image and finds the horizontal coordinate values of the left and right endpoints of all connected domains, and then calculates the horizontal difference between the left and right endpoints of each connected domain. As sea-sky line has the features uninterrupted along a certain direction and strong texture features, the connected domain corresponding to the largest difference is most likely to be a real sea-sky line. The experimental results show that since the ship also has the similar texture characteristics with the sea-sky line, it is easy to be interfered by the ship when the threshold value is less than 0.73 * width and cause misjudgment. When the threshold value is greater than 0.83 * width, missed judgments may occur due to the unobvious texture characteristics of the sea-sky line. Therefore, this paper selects the median value of 0.78 * width. For more comprehensive considerations, when the connected domains with the same difference value are all larger than threshold, we select the suspicious target located at the top in the image as the final sea-sky line, the least square method is used to fit the points in the refined sea-sky line after determining sea-sky environment. Finally, detection of the sea-sky line is realized.

Because we have detected that sea-sky line basically exists in two ways, one is nearly horizontal direction, the other is inclined direction. We choose different area segmentation rules for different situations. When the vertical distance between left end point and right end point of the sea-sky line is less than 5 pixels, we will move the sea-sky line vertically up and down 5 pixels respectively to segment the image. When it is greater than or equal to 5, the segmentation rule is to divide image area with left and right endpoints as boundary points. So as to divide the sky area, sea-sky area and maritime area.

B. DETECTION METHOD OF INFRARED SEA-SKY TARGET

From the analysis and summary of the Section II, it can be seen that the infrared target in the sea-sky area occupies a small number of pixels, most of which are small and weak targets. The contour is more obscure and gray value does not have an absolute advantage in the whole image. However, the gray level and contrast information of the target in the sea-sky area are the most saliency. In this paper, a PLS method is proposed. Firstly, the image is convoluted with the peak filter to detect the peak point, that is, the suspected position of the target *ConvK* as follow:

$$ConvK = \frac{1}{W * H - 1} \begin{bmatrix} -1 & \cdots & -1 \\ \ddots & & \iddots \\ \vdots & W * H - 1 & \vdots \\ \iddots & & \ddots \\ -1 & \cdots & -1 \end{bmatrix} \quad (4)$$

where W and H represents the length and width of the filter respectively, and W * H determines the scale of the filter. As sea-sky area is basically weak and small target, when W = H = 3, it has a good peak extraction effect. As shown in Fig.6 (a2) - (d2). Secondly, in order to further ''pop out'' real target from suspected target, find the position corresponding to the suspected target point in the original map and calculate mean value u and variance σ to get the threshold value ATV. The adjustable weight factor T directly determines the linear growth of threshold, and T is used to control the degree of interference elimination. It is found from the experiment that when T is greater than 2, it is easy to filter out the weak targets at the sea-sky region. When T is less than 1, there will be more noise interference around the weak targets. This will bring great challenges to the subsequent real target extraction. It has been proved that when T = 1.56, it has the best noise removal effect. Removing part of the interference results through adaptive filtering method (AT) as follow. The results are shown in Fig.6 (a3) - (d3).

$$ATV = T \times \sigma + u \quad (5)$$

At this time, interference point is only the peak point on the sea-sky line. Then, the filtered points on the image are regarded as the potential area of the suspected target and the maximum *mx* and minimum *mn* of the corresponding position in the original image are found. The peak value difference (PD) is obtained as follow:

$$PDV = mx - (mx - mn) \times 0.9 \quad (6)$$

In addition, the foreground and background are divided in the original image by taking peak point as the center, the neighborhood scale as 7 pixels and the threshold value as *PDV*. The local singularity (LS) value *LSV* of each area is calculated, and maximum value is *LSmax* and *LSmin*, *ft* and *bk* represent gray values of foreground and background respectively. *ftcnt* and *bkcnt* express pixels of foreground and background. Which are as follows:

$$LSV = (\text{sum}(ft)/ftcnt)/(\text{sum}(bk)/bkcnt) \quad (7)$$

Finally, the area with the local singularity value greater than (*LSmax* + *LSmin*)/2 is regarded as the final real target detection result and the target point is expanded. The result is shown in Fig.6 (a4) - (d4). The purpose of eliminating the interference of the peak point on the sea-sky line is realized.

C. DETECTION METHOD OF INFRARED MARITIME TARGET

From the analysis and summary of the Section II, it can be seen that the gray scale span of the maritime target is relatively large, and there are more interferences of sea wave clutter. If the PLS is applied, target will be incomplete and the high brightness sea wave clutter may be detected. Therefore, in order to accurately detect the target and reconstruct the original area of the target area, this paper first propose a CEDoG operator, whose core is CEDoG filter, and its

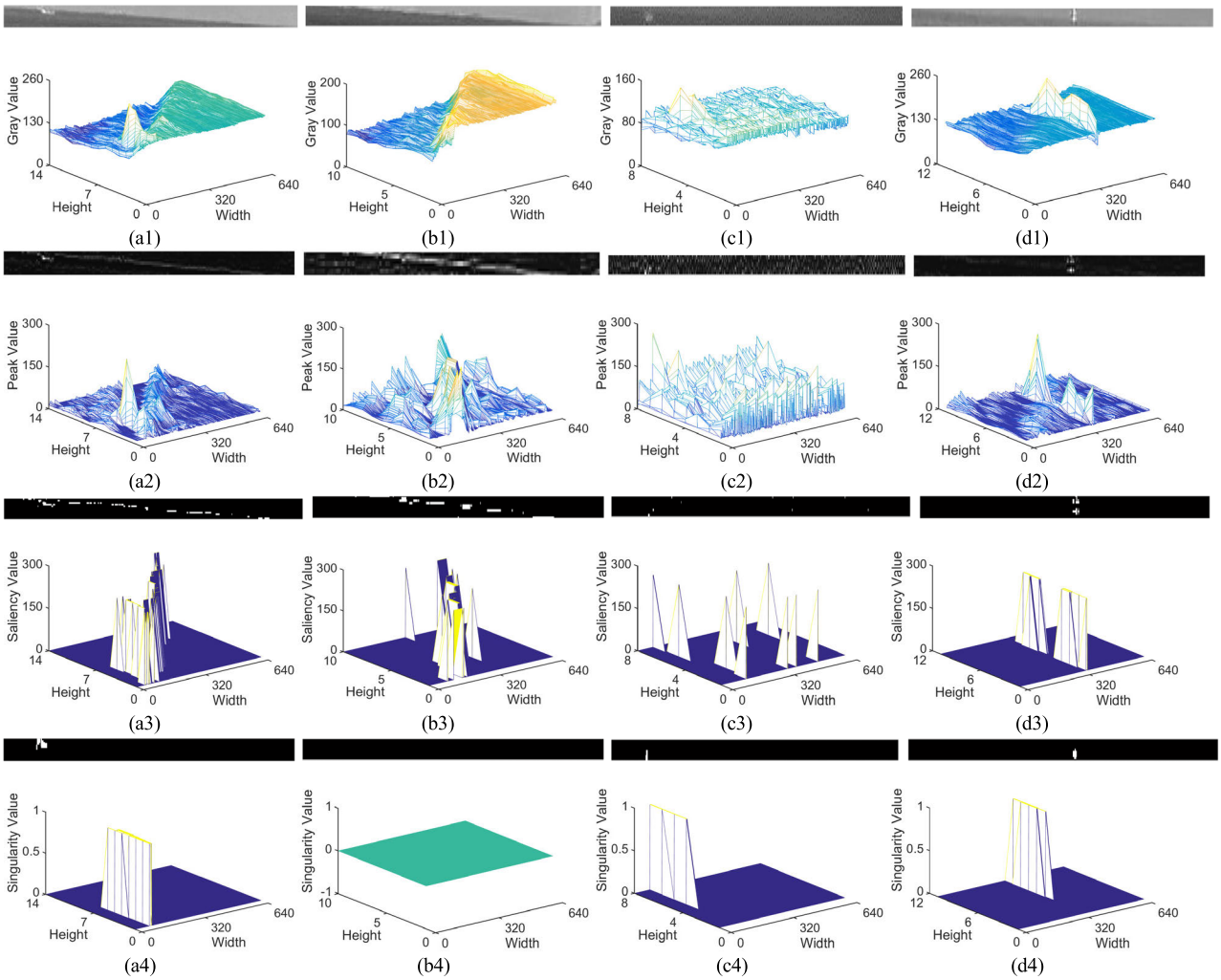

FIGURE 6. (a1)-(d1) Original sea-sky area images. (a2)-(d2) Peak detection results. (a3)-(d3) Adaptive threshold results. (a4)-(d4) Local singularity and expansion results.

two-dimensional expression as follow:

$$CEDoG(x,y) = \frac{1}{2\pi\sigma fe^2}e^{-(x^2+y^2)/(2\sigma fe^2)} - \frac{1}{2\pi\sigma bi^2}e^{-(x^2+y^2)/(2\sigma bi^2)} \quad (8)$$

σbi and σfe are the parameters of foreground enhancement and background suppression respectively. In order to find the most suitable σbi and σfe, this paper analyzes the parameters of the CEDoG filter. Firstly, set the scale in CEDoG to a constant. Secondly, after multiple sets of experimental data, it is found that the processing effect is best when σbi and σfe are the data in Table 3.

Then, the formula (9) is obtained by fitting the above experimental data. Finally, in order to make the CEDoG operator more universally applicable, it is known that the current best calculation method of background estimation σbi is shown in formula (10), so the best calculation method of σfe can be derived as shown in formula (11).

TABLE 3. The σbi and σfe values when the CEDoG processing effect is best.

σbi	10	20	30	40	50
σfe	2.74	2.78	2.82	2.86	2.91
σbi	60	70	80	90	100
σfe	2.95	2.99	3.03	3.07	3.12

$$\sigma fe = \sigma bi/240 + 2.698 \quad (9)$$

$$\sigma bi = 0.5 + S \times 0.15 \quad (10)$$

$$\sigma fe = 2.7 - S/1600 \quad (11)$$

where S is the pixel number of image width. The utility model has a narrow positive central convex groove and an extended negative peripheral groove. The one-dimensional form of CEDoG filter is shown in Fig. 7. CEDoG operator is composed of two different scales of Gaussian low-pass filter

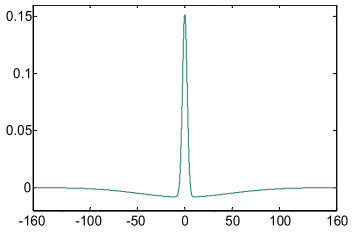

FIGURE 7. 1-D demonstration for CEDoG filter and we set both the filter width and height to be the width of the input image.

difference. The low-scale filter mainly filters out sea wave clutter in high-frequency information. The high-scale Gaussian low-pass filter mainly performs background estimation and then perform a difference operation on the images processed by the two scales, thereby improving the significance of the target.

Fig.8 (a2) - (d2) is the result of CEDoG operator process image. Then we calculate the mean and variance of CEDoG operator processing result and segment the image by adaptive threshold by formula (5), as shown in Fig.8 (a3) - (d3). We find that there are still some strong wave noise points to be separated.

In order to remove the noise points and reconstruct the original area of the target, this paper use H-OTSU method to segment the image.

Step 1: CEDoG processing result is binarized with a H-OTSU method (90% maximum threshold) to generate a seed point as shown in Fig. 8 (a4) - (d4).

Step 2: The seed points are grown in the eight-connected domain on the CEDoG processed image.

Step 3: The seedless point position is determined as the background, and the final growing region is determined as the target position.

From the result Fig.8 (a5) - (d5), it can be found that the proposed algorithm in this paper can achieve accurate detection and retain the original area of the target.

IV. EXPERIMENTAL RESULTS

In this chapter, in order to evaluate the performance index of proposed algorithm more accurately. In Section A, validation data sets is introduced and compared with six kinds of target detection algorithms, which are mutual wavelet energy combination algorithm to improve the target significance under the sea-sky background (WT) [5], multiscale fuzzy metric model for single background suppression (MFMM) [15], robust infrared maritime target detection based on visual attention and spatiotemporal filtering in the complex scene including the sea-sky environment (VAPFM) [10], multiscale patch-based contrast measure for small infrared target detection (MPCM) [20], infrared small target detection via non-convex rank approximation minimization joint l2,1 norm (NRAM) [23] and spatial–temporal local difference measure (STLDM) [42]. At the same time, the detailed parameter settings of seven detection methods are provided. The advantages of the proposed strategy and comparison algorithm in detection results, signal-to-clutter ratio and the background suppression factor, recall and precision, elapsed time and receiver operating characteristic curve (ROC) are analyzed respectively in Section B.

A. DATASET ANALYSIS

In our data sets, there are eight infrared maritime image sequences and 5895 single frames in total. These image sequences were all captured in the sea -sky environment. All images were quantized at an eight-bit resolution and had a size of 640 pixels width and 512 pixels height as shown in Fig. 9. Table 4 shows the experimental environment and image feature description of each image sequence.

In order to analyze the performance advantages of each algorithm more fairly, the detailed parameter settings of the six detection methods are listed in Table 5. According to Table 4 and Fig.9, there may be small or large targets, clear or obscure outline, single target and multiple targets, as well as at the edge and so on in the infrared image of the sea-sky environment. Islands, sea waves, lens flare and clouds are also common background interferences. Sea-sky line exist in horizontal or inclined directions. Therefore, our data sets cover the common challenges in detecting infrared maritime targets in the sea -sky environment and excellent detection performance on these data sets can verify the effectiveness of the algorithm.

B. FINAL RESULTS AND PERFORMANCE COMPARISON

We provide a representative original image for each image sequence. The intermediate process and detection results of the proposed strategy as shown in Fig.9. From the above experimental results, it can be known that the position of sea-sky line can be detected accurately. The sea-sky area will find the potential area of the target after PD and AT methods, but there will be a lot of background noise at the same time, and then, the position of the target can be accurately determined after LS method. The maritime area target's saliency will be improved after the CEDoG method, and the background noise's saliency will be weakened. The AT method can be used to find the target's potential area. Finally, the H-OTSU and area growth can accurately detect the target and maintain the original outline area of the target.

In order to reflect the versatility of the proposed algorithm, the data set in Fig.10 is used to enrich the types of test images. For the convenience of observation, the target is marked with a red box. It can be found that the proposed method can accurately detect multiple targets in the maritime and sea-sky area. Even if there is island interference, the target can still be detected. In order to illustrate the effectiveness of our algorithm, we conducted comparative experiments.

The comparison detection results are shown in Fig 11. WT method can accurately detect the target in Fig.11 SeqC and SeqH. Because WT method is more sensitive to horizontal and vertical gradients, it will produce more interference in the above analysis environment. For example, data

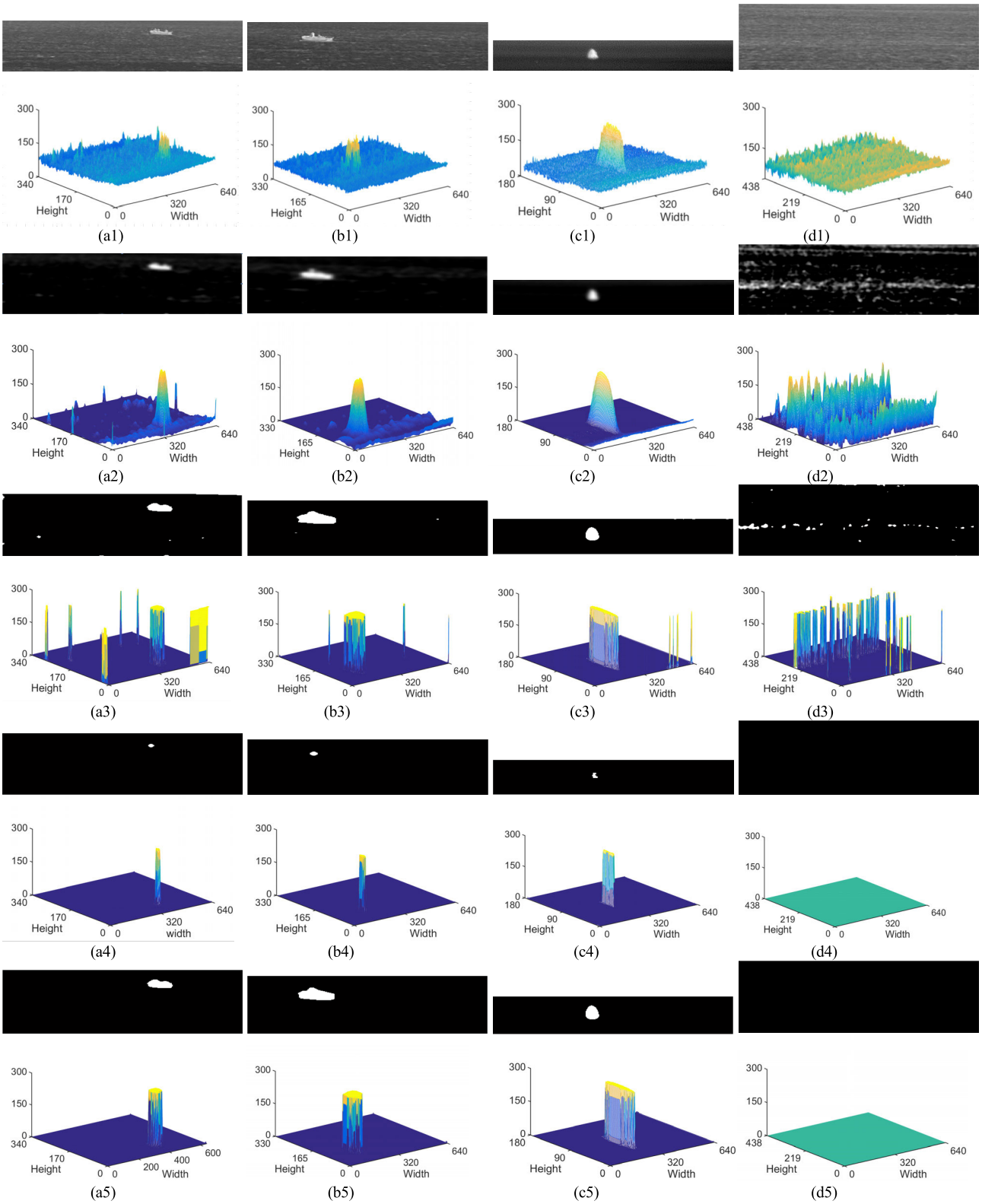

FIGURE 8. (a1)-(d1) Original maritime area images. (a2)-(d2) CEDoG operator processing result. (a3)-(d3) Adaptive threshold results. (a4)-(d4) H-OTSU methods processing result. (a5)-(d5) Maritime targets detection result.

sets in Fig.11 SeqB, SeqE and SeqF, because the target has strong interference texture features in both horizontal and vertical directions as well as in some sea waves, the target can be detected accurately and accompanied by wave clutter, although the target is not lost, there are false targets. For Fig.11 SeqA, SeqD and SeqG, the overall texture features

TABLE 4. Experimental environment and feature description of each image sequence.

Image sequence	Number of test sets	Experimental environment description			Image description			
		Wind Speed(m/s)	Wave Height(m)	Infrared Camera	Number of targets	Target feature	Background interference	Sea-sky Line Direction
A	500	3.6-4.0	0.4-0.5	Medium wave refrigeration	2	Weak small targets and contour clear target	Sea waves	→
B	826	5.0-5.4	0.4-0.6	Long wave un-refrigeration	2	Weak small targets	Cloud Sea waves	↗
C	301	1.6-2.8	0.1-0.3	Medium wave refrigeration	2	Weak small targets and one near the border	Lens flare Sea waves	→
D	500	5.2-5.6	0.5-0.6		2		Sea waves	
E	1060	3.2-3.8	0.3-0.5		2	Contour clear target	Cloud Islands Sea waves	
F	520	5.0-5.4	0.4-0.6	Long wave un-refrigeration	1	Weak small targets	Cloud Sea waves	
G	1188	3.7-4.0	0.4-0.5	Medium wave refrigeration	4	Weak small targets and contour clear target	Cloud Sea waves	→
H	1000	5.2-5.6	0.5-0.6		1	Weak small targets	Islands Sea waves	

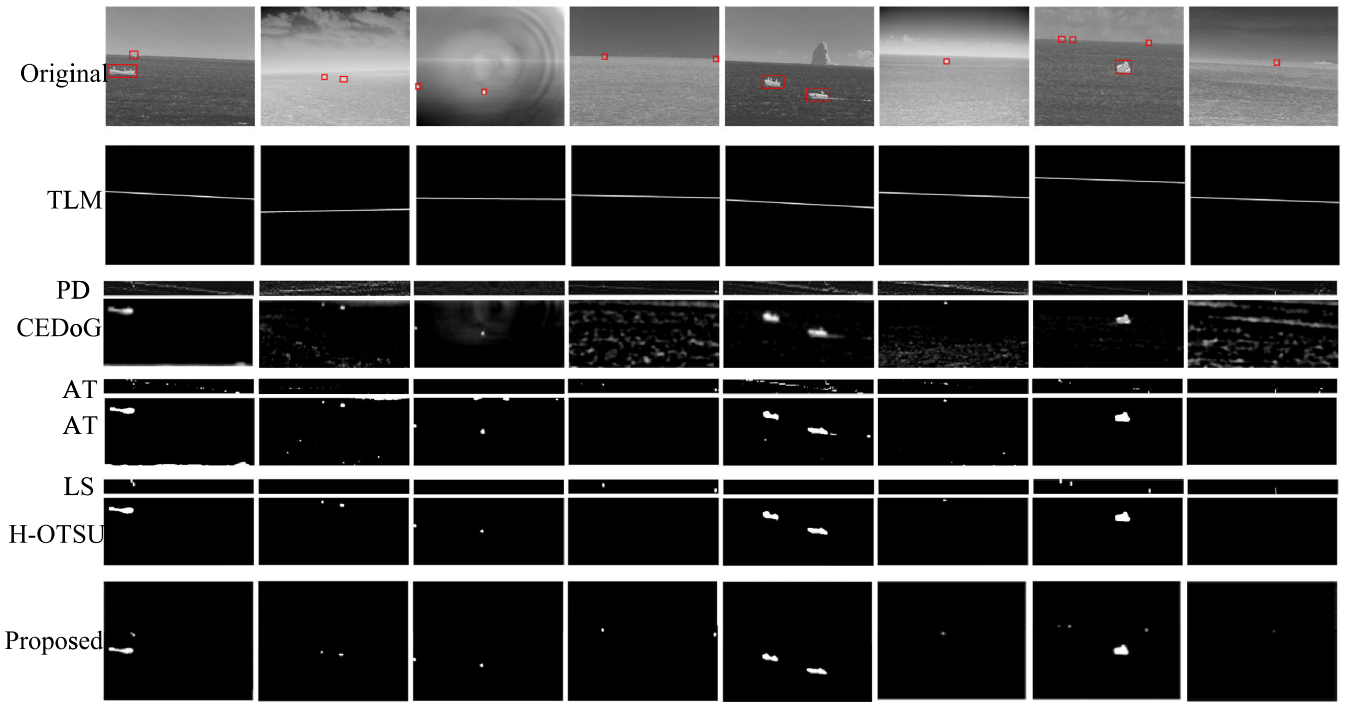

FIGURE 9. The experimental process and results of our algorithm.

of the small target are not prominent enough, part of the target is detected, which does not achieve the goal of accurate detection of the target. The idea of MFMM is to transform the target detection task into measure issue of portraying such correlation/noncorrelation properties, which can be availably solved using the MFMM that measures the certainty of targets in images. The key of MFMM is the selection of the optimal window size. It can be found from the data sets in Fig.11 SeqF

TABLE 5. Detailed parameter settings of the six detection methods.

No.	Methods	Abbreviations	Parameter Settings
1	Mutual wavelet energy combination using wavelet transform	WT	Wavelet base: haar. A slide 6×6 pixels window. The threshold value of judgment of horizontal or oblique is 20.
2	Multiscale fuzzy metric model	MFMM	Entropy of a 9×9 windows. The alpha value of segmented target is 0.4 to 0.6.
3	Visual attention and pipeline-filtering model	VAPFM	Classification threshold :0.016. Block Size:32×32.
4	Multiscale patch-based contrast measure	MPCM	N = 3, 5, 7, 9. Mean filter size: 3 × 3.
5	Non-convex rank approximation minimization joint l2,1 norm	NRAM	g norm:0.002. Patch size: 50 × 50. Sliding step: 10.
6	Spatial–temporal local difference measure	STLDM	Subblock measures 3 × 3 pixels. K=10.
7	PLS and CEDoG	Proposed	Neighborhood scale as 7. T=1.56. Filter size 3×3.

and SeqH that small targets can be successfully detected without false targets after the optimal window is determined. although the target is not lost, there are false targets for Fig.11 SeqB,

SeqD and SeqE. For Fig.11 SeqA and SeqG with small and large targets at the same time, small target is no strong continuity feature, which also leads to missed detection. VAPFM is always an efficient method of target detection. For the data sets Fig.11. SeqB, SeqE, SeqF and SeqH, once there is a cloud or island interference, there is a false alarm. When the radiation intensity of the cloud or island is stronger, there is a missed alarm for Fig.11 SeqB and SeqH. Fig.11 SeqA and SeqG with small and large targets at the same time, small targets are easily missed. It can be seen from the MPCM detection results that is also vulnerable to the interference of waves and clouds, as shown in Fig. 11 SeqA, SeqB, SeqD, SeqE and SeqG. NRAM has a better detection effect than other methods, but when the target is small and the sea waves noise is strong, there will be a certain false target, as shown in Fig.11 SeqA, SeqE, SeqG and SeqH. STLDM method is very sensitive to local highlights, a large number of false alarms are generated in Fig. 11. SeqA, SeqB, SeqD, SeqE, SeqF and SeqH. Therefore, based on the detection results, it can be seen that WT algorithm can overcome the

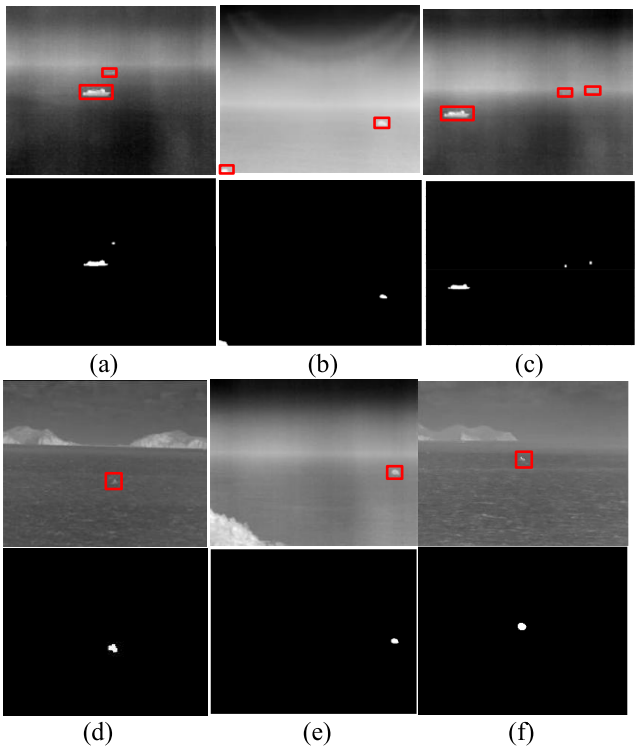

FIGURE 10. Experimental results of our algorithm. ((a)-(c) small wind waves, (d)-(f) Island interference).

interference of large size such as islands and clouds, but it is more sensitive to waves and prone to false alarm. When the target is large, if the edge of the target has strong texture characteristics, it can be successfully detected. It will be missed when target is weak, Therefore, the robustness of the algorithm needs to be improved. For the MFMM and VAPFM method, although it can well suppress the interference of sea wave, but when large targets appear, small targets are easy to lose. For the MPCM, NRAM and STLDM method, although algorithm has a low false alarm rate, there are strong interferences from sea waves noise, more false targets will appear.

We select the signal-to-clutter ratio gain (SCRG) and the background suppression factor (BSF) as evaluation indices. The SCRG and the BSF are defined as:

$$SCRG = \frac{(S/C)_{out}}{(S/C)_{in}} \tag{12}$$

$$BSF = \frac{C_{in}}{C_{out}} \tag{13}$$

where S and C are the average target intensity and clutter standard deviation respectively. The $(\cdot)$ in and $(\cdot)$ out are the original image and the result of the method. The SCRG index measures the magnification of target relative to the backgrounds before and after processing. The BSF represents the suppression effect of backgrounds without any information about the target.

Experimental results of these methods with the index are shown in Table 6. The highest value of each evaluation index

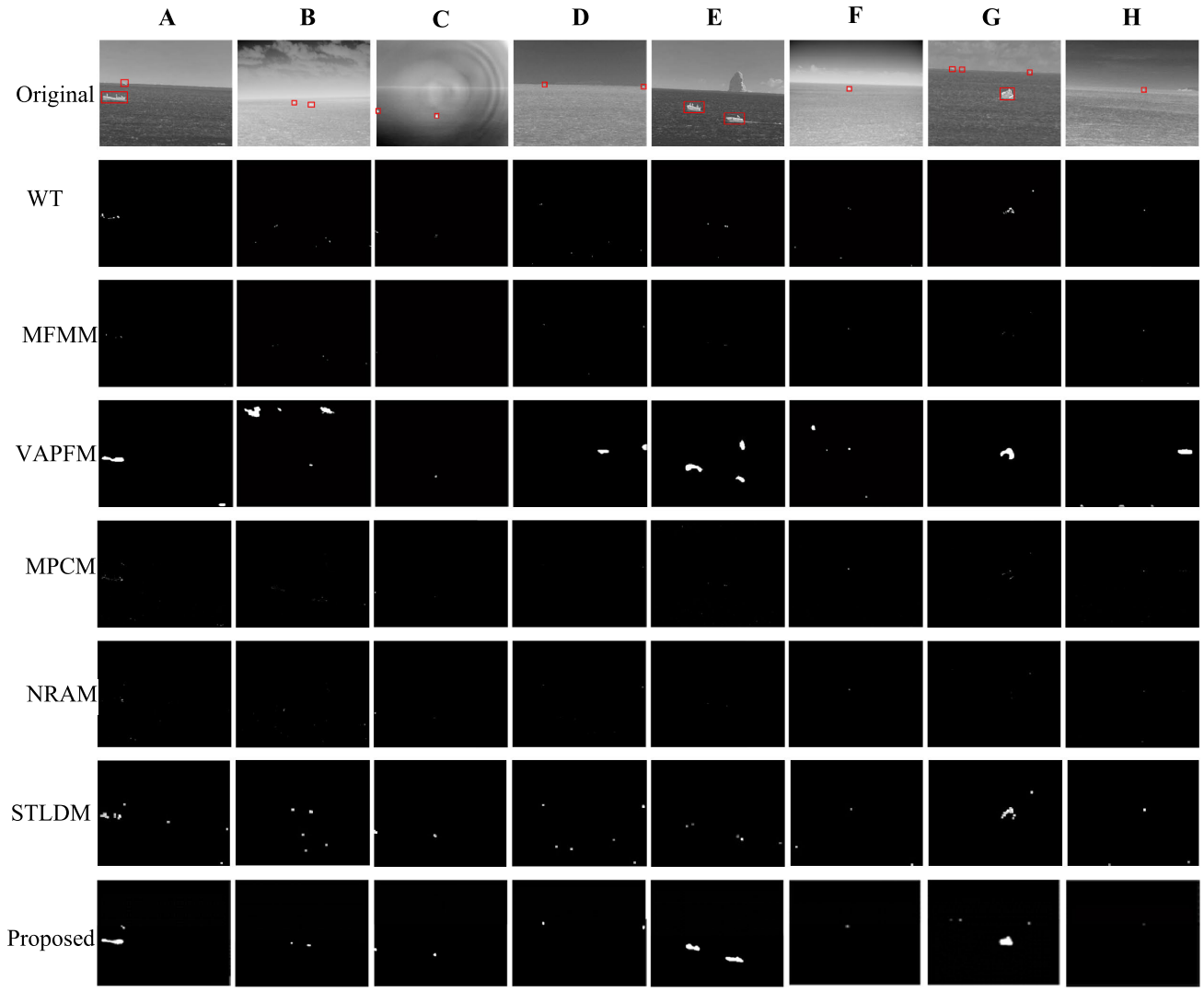

FIGURE 11. Comparison of detection results of different detection algorithms.

TABLE 6. Evaluation indices comparison of SCRG, BSF.

Method	Evaluation Indices	A	B	C	D	E	F	G	H
Proposed	SCRG	10.17	10.20	12.41	8.50	8.17	9.54	14.51	8.17
	BSF	8.91	9.75	10.82	7.78	6.47	9.68	6.95	6.47
WT	SCRG	4.21	7.91	15.31	4.89	3.31	5.21	4.31	3.81
	BSF	4.22	3.57	2.15	4.15	2.24	2.43	3.12	2.19
MFMM	SCRG	2.97	3.95	3.15	3.95	1.51	3.17	2.77	1.71
	BSF	2.78	8.91	8.31	2.71	2.87	7.41	2.42	2.46
VAPFM	SCRG	3.51	4.12	2.09	4.62	5.53	4.51	3.65	5.79
	BSF	4.79	3.21	6.17	3.27	5.02	3.47	4.31	4.02
MPCM	SCRG	4.21	2.12	9.51	2.79	3.63	4.17	4.91	6.63
	BSF	4.41	3.45	8.10	3.82	3.12	4.21	4.81	6.22
NRAM	SCRG	6.18	4.95	9.98	6.94	4.05	6.17	3.65	4.16
	BSF	6.76	8.62	8.12	8.19	3.92	7.31	5.31	3.85
STLDM	SCRG	4.17	5.18	6.75	3.15	4.45	5.75	4.31	5.34
	BSF	4.83	5.61	6.78	3.29	4.27	5.97	4.28	5.31

in each column is marked red, and the second-highest one is marked blue.

From Table 6, it can be seen that the proposed method achieves the highest values of SCRG and BSF in SeqA, SeqB, SeqE, SeqF, SeqG and SeqH. The proposed method can improve SCRG to some extent, it means the detected target is more prominent than the backgrounds while achieving a better suppression effect on the background. That is to say, the proposed method outperforms the compared methods in both target enhancement and background suppression from the angle of numerical indicator values for these data sets. For SeqC, the proposed method has the second highest SCRG, which is smaller than WT method because the method more suitable for small targets in smooth sea surface. Although the SCRG of WT method is higher than that of proposed method, the BSF of WT method is far lower than that of the proposed strategy, which means that the detection results are easy to generate noise. For SeqD, although NRAM has the highest BSF, SCRG is far less than the proposed method in this paper, so the significance of the target may be covered up. The main reason is that there are just sea wave noises, and NRAM detection strategy is more suitable for filter sea wave interference. In general, the proposed method in this paper can achieve the best detection effect.

TABLE 7. Evaluation indices comparison of Recall, Precision.

Method	Evaluation Indices	A	B	C	D	E	F	G	H
Proposed	Recall(%)	96.8	100.0	100.0	100.0	100.0	99.3	95.0	99.9
	Precision(%)	90.2	94.3	97.0	97.2	97.7	94.7	89.4	95.8
WT	Recall(%)	60.5	94.2	91.3	44.7	29.3	80.8	45.7	75.7
	Precision(%)	35.8	63.5	57.3	30.4	29.9	39.5	80.4	70.4
MFMM	Recall(%)	63.7	76.5	90.4	81.9	34.4	80.3	11.9	11.9
	Precision(%)	36.8	74.3	69.1	69.5	52.7	89.5	80.4	90.4
VAPFM	Recall(%)	63.7	53.3	66.7	65.7	91.5	85.5	42.9	42.9
	Precision(%)	37.8	46.4	68.3	50.4	90.7	80.7	75.2	75.2
MPCM	Recall(%)	80.9	84.2	90.6	75.7	81.9	70.1	81.9	80.7
	Precision(%)	60.5	83.5	97.3	70.4	65.5	70.5	79.5	80.8
NRAM	Recall(%)	83.5	94.3	90.0	96.0	89.0	88.3	90.3	90.2
	Precision(%)	89.6	86.5	92.6	97.5	79.5	90.7	86.7	90.3
STLDM	Recall(%)	81.8	94.1	96.2	91.3	80.3	82.5	55.6	80.1
	Precision(%)	51.1	65.7	85.3	61.1	61.6	78.6	76.1	73.3

TABLE 8. Time-consumption comparison of different detection methods on eight test image sequences. (The algorithm run time is calculated based on Visio Studio 2019, installed on Windows 10 Ultimate with an Intel Core i5 9400F processor(3.89GHz) and 8.0GB of RAM).

	A	B	C	D	E	F	G	H
Proposed	0.379	0.291	0.114	0.136	0.286	0.288	0.373	0.106
WT	2.101	1.596	0.969	0.868	1.698	1.915	2.018	0.879
MFMM	0.890	0.593	0.431	0.479	0.596	0.515	0.897	0.479
VAPFM	1.520	1.098	0.895	0.837	0.998	1.054	1.442	0.890
MPCM	0.751	0.698	0.496	0.418	0.618	0.654	0.712	0.419
NRAM	3.189	2.900	1.142	1.248	2.110	2.240	3.425	1.387
STLDM	0.710	0.610	0.670	0.650	0.630	0.700	0.670	0.620

So as to achieve a more detailed study to better show the advantages of the algorithm, new performance indexes in machine learning are cited, Precision and Recall by statistical calculations are defined as:

$$Precision = \frac{TP}{TP + FP} \tag{14}$$

$$Recall = \frac{TP}{TP + FN} \tag{15}$$

TP FP FN is represented as true positive, false positive, false negative. The highest value of each evaluation index in each row is marked red, and the second-highest one is marked blue. Calculation results are shown in Table 7.

The overall recall of the proposed algorithm is larger than other algorithms. For precision, although the SeqC and SeqD is lower than that of MPCM and NRAM, the difference is not obvious. For other sequences, the proposed method is significantly higher than the comparison methods. Moreover, to compare the computational cost of the six methods more clearly, we compare the processing time of each method. The minimum value of each evaluation index in each column is marked red, and the second- lowest one is marked blue is shown in Table 8.

We can observe that the proposed method has the shortest time consumption compared with other methods. Table 9 shows the algorithm complexity. Suppose the image size is and m, n are the rows and columns of the patch-image. The computational cost of WT is $O(mn \log mn)$, The main time-consuming part is wavelet decomposition. The computational cost of proposed method, STLDM and MFMM are $O(l^2 \log l^2)$, where the l^2 is the size of the optimal window. Considering the image size, the final cost of proposed method and MFMM are $O(l^2 \log l^2 mn)$. For VAPFM and MPCM, it is obvious that the major time-consuming part is calculating the saliency map pixel by pixel. A sliding window of size is needed for computing the saliency value of the central pixel. Thus, k^2 times mathematical operation per pixel is required, namely, in a single scale, the computational cost is $O(k^2 mn)$. Therefore, the total cost in all scales is $O(k^3 mn)$. For the NRAM methods, the dominant factor is singular value decomposition (SVD), which has a computational complexity of $O(mn^2)$.

TABLE 9. Comparison of computational complexity of six methods.

	Proposed	WT	MFMM
Complexity	$O(l^2 \log l^2)$	$O(mn \log mn)$	$O(l^2 \log l^2)$
	VAPFM	MPCM	NRAM
Complexity	$O(k^2 mn)$	$O(k^3 mn)$	$O(mn^2)$
	STLDM		
Complexity	$O(l^2 \log l^2)$		

To further demonstrate the advantages of the developed method, we provide the ROC curves of the test sequences used in Fig.12, by counting number of false alarm pixels *NFAP*, total number of pixels in the whole image *NPI*, number of real targets detected pixels *NTDP* and total number of real target pixels *NTP*. False alarm rate *FAR* and detection rate *DR* for different infrared images are calculated, expressed as:

$$FAR = \frac{NFAP}{NPI} \tag{16}$$

$$DR = \frac{NTDP}{NTP} \tag{17}$$

The results show that the WT method is susceptible to interference from sea waves and is a very unstable method. For MFMM, the choice of the optimal window size determines the final detection effect. Therefore, it is difficult to have a stable detection effect on targets in different sea-sky environments. VAPFM always performed the worst since the it is poor at addressing scenes filled with clouds and islands. The performance of MPCM fluctuated greatly. For SeqC, SeqF and SeqH, MPCM worked well but failed in the other sequences, which confirmed that MPCM is powerless in dealing with scenes filled with clutters. The ROC performance index of NRAM method is basically the same as that of proposed method. But when the target is small and the wave is strong, such as SeqA, SeqF, SeqG and SeqH, if you want to reach the maximum DR, you need to generate a larger FAR. The biggest disadvantage of STLDM method is that it is sensitive to highlight points, which makes it produce large FAR. In conclusion, when compared with the same FAR, the proposed method almost achieves the highest DR, which means that proposed method is superior to other state-of-the-art methods.

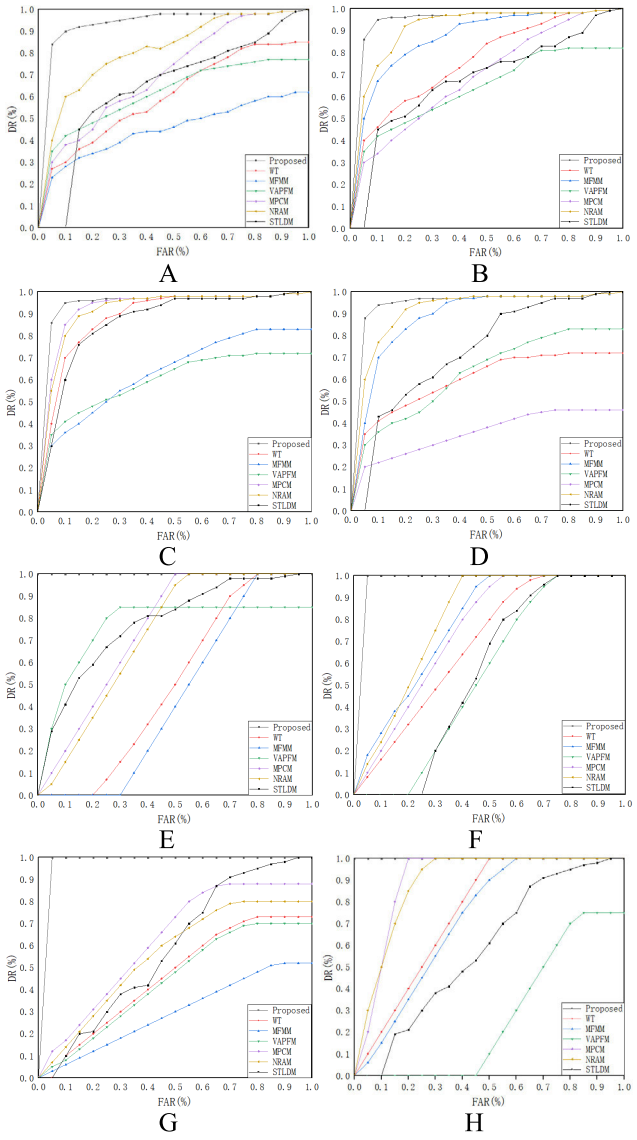

FIGURE 12. ROC curves of detection results of eight real sequences.

V. CONCLUSION

In this paper, a method of distinguishing the sea-sky environment and detecting the infrared target is proposed. According to analysis, the features of different area targets, consists of three key units: In the process of judging and extracting sea-sky line, a TLM method is proposed with the purpose of refining sea-sky area to achieve precise locating of the sea-sky line. In the procedure of detecting sea-sky target, in order to "pop out" target and restrain the interference of the sea wave, a PLS strategy is applied. In the step of maritime target segmentation, the automatic segmentation method is selected. CEDoG filtering method is adopted to enhancing the saliency of the target, and combine H-OTSU and area growth method to keep full target areas. To evaluate the performance of proposed method, we captured eight different image sequences (5895 frames in total) under a variety of sea-sky environments. Proposed method is robust in enhancing the values of SCRG and BSF of the images, higher accuracy and recall rate, shorter elapsed time, lower complexity and has superior performance in terms of the detection rate and false alarm rate.

REFERENCES

[1] S. Aghaziyarati, S. Moradi, and H. Talebi, "Small infrared target detection using absolute average difference weighted by cumulative directional derivatives," *Infr. Phys. Technol.*, vol. 101, pp. 78–87, Sep. 2019.

[2] D. Tang, G. Sun, D.-H. Wang, Z.-D. Niu, and Z.-P. Chen, "Research on infrared ship detection method in sea-sky background," in *Proc. Int. Symp. Photoelectron. Detection Imag., Infr. Imag. Appl.*, Sep. 2013, p. 8907.

[3] L. Peng, T. Zhang, S. Huang, T. Pu, Y. Liu, Y. Lv, Y. Zheng, and Z. Peng, "Infrared small-target detection based on multi-directional multi-scale high-boost response," *Opt. Rev.*, vol. 26, no. 6, pp. 568–582, Dec. 2019.

[4] S. Li, X. Ai, R. Wu, and N. Zeng, "Infrared target edge detection in sea sky backgrand," *IEEE Access*, pp. 1234–1238, 2017.

[5] X. Kong, L. Liu, Y. Qian, and M. Cui, "Automatic detection of sea-sky horizon line and small targets in maritime infrared imagery," *Infr. Phys. Technol.*, vol. 76, pp. 185–199, May 2016.

[6] B. Wang, L. Dong, M. Zhao, H. Wu, and W. Xu, "Texture orientation-based algorithm for detecting infrared maritime targets," *Appl. Opt.*, vol. 54, no. 15, p. 4689, May 2015.

[7] N. Imamoglu, W. Lin, and Y. Fang, "A saliency detection model using low-level features based on wavelet transform," *IEEE Trans. Multimedia*, vol. 15, no. 1, pp. 96–105, Jan. 2013.

[8] Y. Lu, S. Huang, and W. Zhao, "Sparse representation based infrared small target detection via an online-learned double sparse background dictionary," *Infr. Phys. Technol.*, vol. 99, pp. 14–27, Jun. 2019.

[9] P. Zhang, X. Wang, X. Wang, C. Fei, and Z. Guo, "Infrared small target detection based on spatial-temporal enhancement using quaternion discrete cosine transform," *IEEE Access*, vol. 7, pp. 54712–54723, 2019.

[10] L. Dong, B. Wang, M. Zhao, and W. Xu, "Robust infrared maritime target detection based on visual attention and spatiotemporal filtering," *IEEE Trans. Geosci. Remote Sens.*, vol. 55, no. 5, pp. 3037–3050, May 2017.

[11] S. Tunc and H. A. Ilgin, "Dim target detection in infrared images using saliency algorithms," *Radioengineering*, vol. 27, no. 3, pp. 635–642, Sep. 2019.

[12] L. Dong, D. Ma, G. Qin, T. Zhang, and W. Xu, "Infrared target detection in backlighting maritime environment based on visual attention model," *Infr. Phys. Technol.*, vol. 99, pp. 193–200, Jun. 2019.

[13] Y. Chen, B. Song, X. Du, and M. Guizani, "Infrared small target detection through multiple feature analysis based on visual saliency," *IEEE Access*, vol. 7, pp. 38996–39004, 2019.

[14] J. Han, Y. Ma, J. Huang, X. Mei, and J. Ma, "An infrared small target detecting algorithm based on human visual system," *IEEE Geosci. Remote Sens. Lett.*, vol. 13, no. 3, pp. 452–456, Mar. 2016.

[15] H. Deng, X. Sun, and X. Zhou, "A multiscale fuzzy metric for detecting small infrared targets against chaotic cloudy/sea-sky backgrounds," *IEEE Trans. Cybern.*, vol. 49, no. 5, pp. 1694–1707, May 2019.

[16] S. Zhang, F. Huang, B. Liu, H. Yu, and Y. Chen, "Infrared dim target detection method based on the fuzzy accurate updating symmetric adaptive resonance theory," *J. Vis. Commun. Image Represent.*, vol. 60, pp. 180–191, Apr. 2019.

[17] C. L. P. Chen, H. Li, Y. Wei, T. Xia, and Y. Y. Tang, "A local contrast method for small infrared target detection," *IEEE Trans. Geosci. Remote Sens.*, vol. 52, no. 1, pp. 574–581, Jan. 2014.

[18] Y.-P. Deng and M. Wang, "The small infrared target detection based on visual contrast mechanism," in *Proc. Design, Manuf. Mechatronics*, Nov. 2015, pp. 962–966.

[19] Y. Qin and B. Li, "Effective infrared small target detection utilizing a novel local contrast method," *IEEE Geosci. Remote Sens. Lett.*, vol. 13, no. 12, pp. 1890–1894, Dec. 2016.

[20] Y. Wei, X. You, and H. Li, "Multiscale patch-based contrast measure for small infrared target detection," *Pattern Recognit.*, vol. 58, pp. 216–226, Oct. 2016.

[21] Y. Li, Y. Zhang, J.-G. Yu, Y. Tan, J. Tian, and J. Ma, "A novel spatio-temporal saliency approach for robust dim moving target detection from airborne infrared image sequences," *Inf. Sci.*, vol. 369, pp. 548–563, Nov. 2016.

[22] J. Han, Y. Ma, B. Zhou, F. Fan, K. Liang, and Y. Fang, "A robust infrared small target detection algorithm based on human visual system," *IEEE Geosci. Remote Sens. Lett.*, vol. 11, no. 12, pp. 2168–2172, Dec. 2014.
[23] L. Zhang, L. Peng, T. Zhang, S. Cao, and Z. Peng, "Infrared small target detection via non-convex rank approximation minimization joint $l_{2,1}$ norm," *Remote Sens.*, vol. 10, no. 11, p. 1821, 2018.
[24] H. Zhu, S. Liu, L. Deng, Y. Li, and F. Xiao, "Infrared small target detection via low-rank tensor completion with top-hat regularization," *IEEE Trans. Geosci. Remote Sens.*, vol. 58, no. 2, pp. 1004–1016, Feb. 2020.
[25] Y. Li, Y. Zhang, X. Huang, and A. L. Yuille, "Deep networks under scene-level supervision for multi-class geospatial object detection from remote sensing images," *ISPRS J. Photogramm. Remote Sens.*, vol. 146, pp. 182–196, Dec. 2018.
[26] C. Tao, L. Mi, Y. Li, J. Qi, Y. Xiao, and J. Zhang, "Scene context-driven vehicle detection in high-resolution aerial images," *IEEE Trans. Geosci. Remote Sens.*, vol. 57, no. 10, pp. 7339–7351, Oct. 2019.
[27] R. H. R. Pruim, A. Van Opbroek, M. Kruithof, R. J. M. Den Hollander, J. Baan, S. P. Van den Broek, N. Van der Stap, and J. Dijk, "Spatiotemporal detection of maritime targets using neural networks," *Proc. SPIE*, vol. 11169, Sep. 2019, Art. no. 1116905.
[28] Y. Hu, K. Zhang, and C. Xing, "Small and dim ship target detection based on sea-sky-line," *J. Northwestern Polytech. Univ.*, vol. 37, no. 1, pp. 35–40, Feb. 2019.
[29] J. Ryu and S. Kim, "Heterogeneous gray-temperature fusion-based deep learning architecture for far infrared small target detection," *J. Sensors*, vol. 2019, pp. 1–15, Aug. 2019.
[30] S. Zhao, Y. Song, Y. Zhao, Y. Li, L. Li, Q. Hao, and M. Li, "Infrared target detection method based on the receptive field and lateral inhibition of human visual system," *Appl. Opt.*, vol. 56, no. 30, p. 8555, Oct. 2017.
[31] S. Qi, G. Xu, Z. Mou, D. Huang, and X. Zheng, "A fast-saliency method for real-time infrared small target detection," *Infr. Phys. Technol.*, vol. 77, pp. 440–450, Jul. 2016.
[32] M. Wan, G. Gu, W. Qian, K. Ren, and Q. Chen, "Robust infrared small target detection via non-negativity constraint-based sparse representation," *Appl. Opt.*, vol. 55, no. 27, p. 7604, Sep. 2016.
[33] Y. Chen and Y. Xin, "An efficient infrared small target detection method based on visual contrast mechanism," *IEEE Geosci. Remote Sens. Lett.*, vol. 13, no. 7, pp. 962–966, Jul. 2016.
[34] S. Kim and J. Lee, "Scale invariant small target detection by optimizing signal-to-clutter ratio in heterogeneous background for infrared search and track," *Pattern Recognit.*, vol. 45, no. 1, pp. 393–406, Jan. 2012.
[35] K. Zhang, K. Yang, S. Li, and H.-B. Chen, "A difference-based local contrast method for infrared small target detection under complex background," *IEEE Access*, vol. 7, pp. 105503–105513, 2019.
[36] F. Zhou, Y. Wu, Y. Dai, P. Wang, and K. Ni, "Graph-regularized Laplace approximation for detecting small infrared target against complex backgrounds," *IEEE Access*, vol. 7, pp. 85354–85371, 2019.
[37] Y. Sun, J. Yang, Y. Long, Z. Shang, and W. An, "Infrared patch-tensor model with weighted tensor nuclear norm for small target detection in a single frame," *IEEE Access*, vol. 6, pp. 76140–76152, 2018.
[38] J. Gao, Z. Lin, and W. An, "Infrared small target detection using a temporal variance and spatial patch contrast filter," *IEEE Access*, vol. 7, pp. 32217–32226, 2019.
[39] Y. Sun, J. Yang, Y. Long, and W. An, "Infrared small target detection via spatial-temporal total variation regularization and weighted tensor nuclear norm," *IEEE Access*, vol. 7, pp. 56667–56682, 2019.
[40] Z. Liu, X. Bai, C. Sun, F. Zhou, and Y. Li, "Multi-modal ship target image smoothing based on adaptive mean shift," *IEEE Access*, vol. 6, pp. 12573–12586, 2018.
[41] C. G. Ribbing, "Temperature correction of radiometric emission factors for nongray objects," *Opt. Eng.*, vol. 36, no. 12, p. 3416, Dec. 1997.
[42] P. Du and A. Hamdulla, "Infrared moving small-target detection using spatial–temporal local difference measure," *IEEE Geosci. Remote Sens. Lett.*, vol. 17, no. 10, pp. 1817–1821, Oct. 2020.

DONGDONG MA received the M.S. degree from Dalian Maritime University, Dalian, China, in 2020, where he is currently pursuing the joint Ph.D. degree. He has published three SCI articles on infrared maritime target detection in the last three years. His research interests include infrared maritime image feature analysis and extraction, maritime target detection through digital image processing, maritime rescue, and surveillance via infrared imaging.

LILI DONG (Member, IEEE) was born in Qitaihe, Heilongjiang, China, in 1980. She received the B.S. degree in mechanical design manufacturing and automation and the M.S. degree from the College of Information Science and Technology, Dalian Maritime University (DLMU), Dalian, China, in 2002 and 2004, respectively, and the Ph.D. degree in instrument science and technology from the Harbin Institute of Technology, Harbin, China, in 2008. From 2005 to 2008, she was a Teaching Assistant with the College of Information Science and Technology, DLMU. From 2008 to 2012, she was a Lecturer with the College of Information Science and Technology, DLMU. Since 2012, she has been an Assistant Professor with the Mechanical Engineering Department. She has authored 13 articles and three inventions. Her research interests include multispectral target recognition, tunnel lighting, and photoelectric detection.

WENHAI XU received the B.S. and M.S. degrees in precision instrument and the Ph.D. degree in imprecision instrument from the Harbin Institute of Technology, Harbin, China, in 1982, 1984, and 1991, respectively, and the Ph.D. degree in manufacturing machine from the Tokyo Institute of Technology, Tokyo, Japan, in 1993. From 1986 to 1988, he was a Lecturer with the Harbin Institute of Technology and an Assistant Professor from 1992 to 2001. He was a Professor with the Harbin Institute of Technology for four years since 2001. He was the Project Director with Cannon Inc., Tokyo, from 1993 to 2003. He was also a Research Scientist with System Engineers Company Ltd., Yamato, Japan, from 1995 to 1997. He is currently a Professor of opt-electric information science and engineering with Dalian Maritime University, Dalian, China. In the last ten years, he has directed over 30 research projects and applied ten national patents. He has authored over 80 research articles. His research interests include infrared detection, digital image processing, design of high-resolution optical imaging system, and opt-electronic information processing.